Transition into a phonon glass in crystalline thermoelectric $(Sb_{1-x}Bi_x)_2Te_3$ films

F. Rieger,[1] V. Roddatis,[1] K. Kaiser,[2] G. Bendt,[2] S. Schulz,[2] and C. Jooss[1]
[1]*Institute of Material Physics, University of Göttingen, 37077 Göttingen, Germany*
[2]*Institute of Inorganic Chemistry and Center for Nanointegration Duisburg-Essen (Cenide), University of Duisburg-Essen, 45141 Essen, Germany*

(Received 30 April 2019; accepted 3 January 2020; published 6 February 2020)

Gaining fundamental insights into phonon interactions is of high importance for the improvement of thermoelectric materials. The particular challenge is to enable a phonon glass state with low thermal conductivity in crystalline materials with high electron conductivity. We present here the relation between atomic structure and c-axis lattice thermal conductivity $\kappa_{c,l}(T)$ of epitaxially grown nearly single crystalline $(Sb_{1-x}Bi_x)_2Te_3$ thin films. Aberration corrected high-resolution transmission electron microscopy shows a highly ordered crystalline lattice, with doping dependent statistical occupation of the Sb sublattice by Bi atoms and a very low density of planar defects. The observed strong decrease of $\kappa_{c,l}(T)$ with doping is due to an increase both of the Rayleigh scattering rate at point defects as well as of the phonon-phonon scattering rate. For $x = 0.24$ a transition to a low, almost temperature independent $\kappa_{c,l}(T)$ is observed, indicating a transition to a phonon glass state. The theoretical calculations reveal that the phonon mean free path is reduced below the phonon wavelength for the majority of phonon frequencies, suggesting a breakdown of the phonon approximation to heat transport due to the strongly anharmonic lattice.

DOI: 10.1103/PhysRevMaterials.4.025402

I. INTRODUCTION

Binary pnictide (Pn) chalcogenides with tetradymite (Te) crystal structure, such as Bi_2Te_3 and Sb_2Te_3, are semiconductors with a large thermoelectric figure of merit, $ZT \sim 1$, close to room temperature [1]. Although they have been successfully applied in Peltier cooling and thermoelectric energy conversion since the 1950s [2], basic material properties such as the nature of bonding, the impact of spin-orbit coupling [3] on properties as well as their anisotropic thermal conductivities are not well understood. In particular, the origin of the relatively low values of the c-axis thermal conductivity with $\kappa_c = 1.9\,\mathrm{Wm^{-1}\,K^{-1}}$ for Sb_2Te_3 [4] and $\kappa_c = 1.2\,\mathrm{Wm^{-1}\,K^{-1}}$ for Bi_2Te_3 [5], and its strong further reduction in $(Sb_{1-x}Bi_x)_2Te_3$ solid solutions remains elusive, since data obtained at nanostructured materials [6,7] does not allow for separating out intrinsic and microstructural effects.

Both Bi_2Te_3 and Sb_2Te_3 exhibit a layered rhombohedral lattice structure ($R\bar{3}m$, space group #166). Along the c direction, quintuple -[Te(I)-Pn-Te(II)-Pn-Te(I)]- stacks ($Pn = Bi$, Sb) are forming a unit cell, where Te(I) and Te(II) represent two types of differently bonded tellurium atoms. Whereas Te(II) is coordinated nearly octahedrally by Pn atoms, Te(I) has three Pn and three Te(I) as nearest neighbors. The bonding between the quintuple stacks, i.e., between Te(I) atoms is considered as of van der Waals (vdW) type and is the origin of easy cleavage of these materials perpendicular to the c axis [8]. In addition, evidence for resonance bonding (RB) within the quintuple units due to sharing of electrons in unsaturated covalent bonds is obtained from theoretical considerations [9]. Both vdW and RB bonding can create soft lattices with pronounced anharmonicity of the bonding potential, leading to low phonon velocity as well as strong phonon-phonon interactions.

A publication of Venkatasubramanian *et al.* in the year 2001 [10] on metal-organic chemical-vapor deposition (MOCVD)-grown Sb_2Te_3/Bi_2Te_3 superlattices (SLs) triggered various studies on improvement of thermoelectric performance in SLs: It claimed a very high ZT value of ~2.4 at 300 K based on a remarkably low lattice thermal conductivity of $0.22\,\mathrm{Wm^{-1}\,K^{-1}}$, determined by extrapolation of the total thermal conductivity of the SLs to zero doping [11]. To date this value could not be reproduced by other research groups. In addition, an instability of these SLs at temperatures above room temperature was demonstrated [12–14], indicating that low c-axis thermal conductivity is due to interdiffusion. Indeed, thermal decay of Sb_2Te_3/Bi_2Te_3 SLs revealed a reduction of the cross-plane thermal conductivity down to $0.6\,\mathrm{Wm^{-1}\,K^{-1}}$, whereas no reduction was found in stable heterostructures [15].

In recent years, experimental [16,17] and theoretical studies [18–20] elucidated a quite pronounced anharmonicity of the atomic bonding potential in Bi_2Te_3 as well as in Sb_2Te_3. This can be expressed in the Grüneisen parameter $\gamma_G = a_V/(C_V K_T)$, which compares the measured volume expansivity to the product of the heat capacity C_V and the lattice compressibility K_T. Measurements give rather moderate values for the binary systems ($\gamma_G = 1.7$ for Sb_2Te_3 and $\gamma_G = 1.5$ for Bi_2Te_3 at 295 K [21]). The observation of a doping induced softening of a transverse optical (TO) phonon mode by Se substitution of Te [16,21] and the resulting decrease of the phonon bandgap between acoustic and optical modes suggests that a strong increase of phonon-phonon interactions in three phonon processes, involving both types of phonons. Such a scenario is discussed in a recent publication as a key factor for low thermal conductivities in RB material systems [22]. In addition, spin-orbit interactions can shift down the energy

of A as well as TO modes in Sb_2Te_3 and thus gives rise to a higher density of phonon states at low energies [23]. Consequently, studying point disorder and anharmonicity induced thermal disorder of lattice planes in the soft direction (c-axis) as a function of doping is of high interest for unraveling the mechanisms of phonon transport in these thermoelectric materials systems.

Our study provides a correlation between atomic structure of crystalline epitaxial $(Sb_{1-x}Bi_x)_2Te_3$ films obtained by high resolution transmission electron microscopy to careful temperature dependent measurements of c-axis lattice thermal conductivity $\kappa_{c,l}(x, T)$. While $\kappa(T)$ data are available for nanocrystalline Sb_2Te_3 [24] and nanocrystalline $(Sb_{1-x}Bi_x)_2Te_3$ samples [6,7] over a wide temperature range, $\kappa(T)$ data for specific crystallographic directions is only available on Sb_2Te_3 single crystals for the a,b plane [25,26]. We are not aware of any $\kappa_c(T)$ measurements for $(Sb_{1-x}Bi_x)_2Te_3$ crystals. We performed theoretical calculations of $\kappa_{c,l}(T)$ based on the Callaway model [27], using complete phonon dispersions for the calculation of the phonon velocity and density of states (see Method section and Supplemental Material). These calculations give access to the doping dependent change of phonon-phonon and Rayleigh point defect scattering rates. The transition to an almost temperature independent low $\kappa_{c,l}(T)$ for $x = 0.24$ and $T = 160$–300 K is described within the minimum lattice thermal conductivity model of Cahill *et al.* [28], a modification of the model of Slack [29], establishing the transition to a phonon glass state for the phonon transport along the c axis.

II. RESULTS

A. Crystallinity of epitaxial $(Sb_{1-x}Bi_x)_2Te_3$ thin films

The c-axis thermal conductivity study is performed at a series of epitaxial c-axis oriented $(Sb_{1-x}Bi_x)_2Te_3$ ($x = 0$, 0.07, 0.12, 0.24, 1) thin films grown by physical vapor deposition (PVD) in a thickness range between 150 and 1100 nm (Table S1 in the Supplemental Material [47]). The epitaxial growth of phase pure c-orientated rhombohedral tetradymite-type films on (0001) Al_2O_3 substrates is confirmed by x-ray diffraction (XRD), showing only the $00l$ ($l = 3, 6, 9, 12\ldots$) reflections, see Fig. S1 in the Supplemental Material [47]. Sharp peaks with a full width of half maximum of $\Delta\omega < 0.2^\circ$ confirm high crystallinity. Exemplary SEM pictures of the Sb_2Te_3 ($x = 0$) film and of the Bi_2Te_3 ($x = 1$) film reveal smooth surfaces as shown in Fig. S2.

The high perfection of the epitaxial growth is confirmed by high-resolution transmission electron microscopy (HRTEM) and scanning transmission electron microscopy (STEM), see Fig. 1. The size of crystal twin domains is usually larger than 500 nm. The films have also a low density of other macroscopic defects such as antiphase boundaries and stacking faults. Some examples are shown in Fig. S3. Very few antiphase boundaries are observed, i.e., planar defects which are formed by the shift of atomic planes formed by Sb and Te atoms.

The density of stacking faults is very low close to the substrate surface (average distance 50–100 nm), and increases slightly with increase of doping from $x = 0$ to $x = 0.24$ as well as with increasing distance from the substrate. Close to the upper surface of the films, the average distance can approach 10 nm. This may be due to a small temperature gradient during film growth in the thermally poor conducting films. The Bi_2Te_3 film shows slightly more extended defects compared to the Bi-doped Sb_2Te_3 films, especially in the upper surface region.

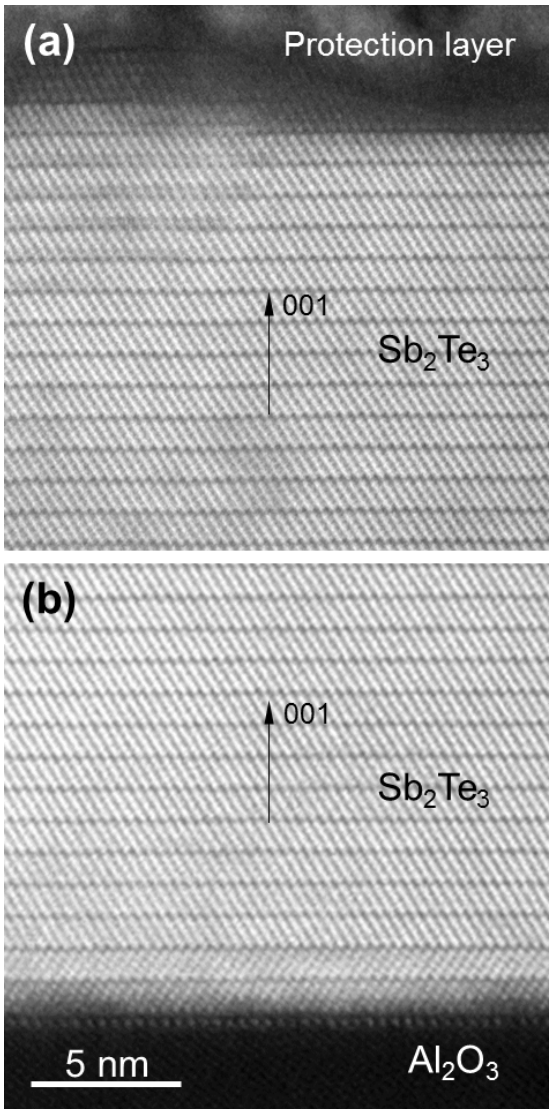

FIG. 1. HRSTEM images of Sb_2Te_3/Al_2O_3 interface and top surface of the Sb_2Te_3 film. The interface reconstruction and twinned areas (2–3 u.c.) close to the Sb_2Te_3/Al_2O_3 interface is sometimes observed. STEM imaging reveals excellent crystallinity of the films, furthermore supported by XRD and local selected area electron diffraction (SAED) patterns shown in the Supplemental Material [47].

B. Solid solution of Bi atoms on *Pn* sites

Figure 2 shows measured and simulated STEM-high-angle annular dark-field (HAADF) results which are in good agreement. Further STEM HAADF images and simulations are presented in the Supplemental Material (Figs. S4 and S5). Bi atoms have a higher atomic number $Z = 83$ and are thus nicely visible in HAADF by their brighter scattering

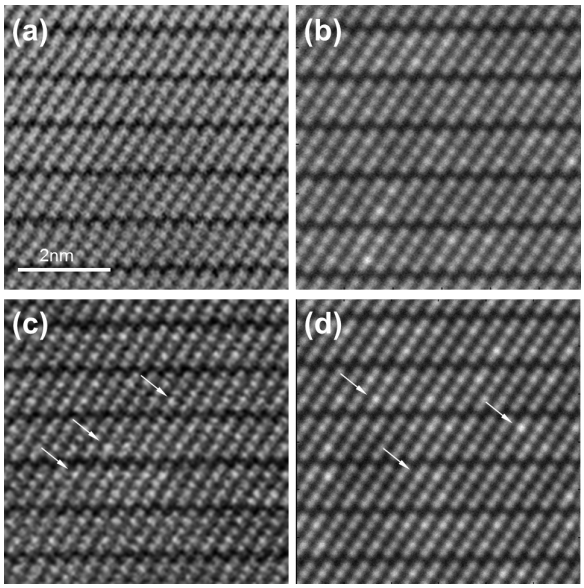

FIG. 2. Experimental HRSTEM HAADF images (zone axis [010]) of $Sb_{0.88}Bi_{0.12}Te_3$ (a) and $Sb_{0.76}Bi_{0.24}Te_3$ (c) as well as simulated images (b) and (d), respectively. A random substitution Bi atoms is used in the simulated image of $Sb_{0.88}Bi_{0.12}Te_3$ films, leading to random appearance of individual bright spots due to atomic columns with higher Bi occupation. The occupation of Sb sites by Bi atoms gives rise to an increased intensity of the *Pn* sites in the quintuple -[Te(I)-*Pn*-Te(II)-*Pn*-Te(I)] layers in (c) and (d) (Sb: $Z = 51$, Te: $Z = 52$, Bi: $Z = 83$). Some examples are marked with the white arrows.

contrast compared to Sb ($Z = 51$) and Te ($Z = 52$). Clearly, Bi occupies the *Pn* sites and is not visible at Te sites. Some contrast variations on *Pn* sites for the $x = 0.24$ is according to the image simulations consistent with statistical occupation of *Pn* columns. The TEM lamellas in Fig. 2 have a thickness of about 15 nm. For $x = 0.24$, this results in an average number of 9 Bi atoms per 35 *Pn* atoms on a column. According to the image simulations, the contrast variation on the *Pn* columns in the experimental HAADF images is consistent with the standard deviation of ± 3 Bi per column and thus proves the presence of a solid solution of Bi atoms on the *Pn* sites.

C. Static point and thermal lattice disorder

Selected area electron diffraction (SAED) patterns reflect high crystallinity of the Sb_2Te_3 and Bi_2Te_3 films, where only the Bragg peaks of the films and the substrate are observed (Fig. S6). For the $(Sb_{1-x}Bi_x)_2Te_3$ solid solutions electron diffraction for $x = 0.12$ and $x = 0.24$ show additional weak spots as well as diffuse streak like diffracted contrast along $(00l)$. A detailed comparison of corresponding spots at $x = 0$ and $x = 0.24$ is shown in Figs. 3(a) and 3(b), respectively. Both reflect the loss of long-range order along the (00l) direction in the solid solutions. The weak additional spots are due to Bi/Sb point disorder on *Pn* columns, which can effectively increase the unit cell along the *c* direction. Since Sb_2Te_3 and Bi_2Te_3 belong to the same space group, the Sb and Bi atoms share the same crystallographic sites in the lattice. The additional spots are consistent with the high-resolution scanning transmission electron microscopy (HRSTEM) images with

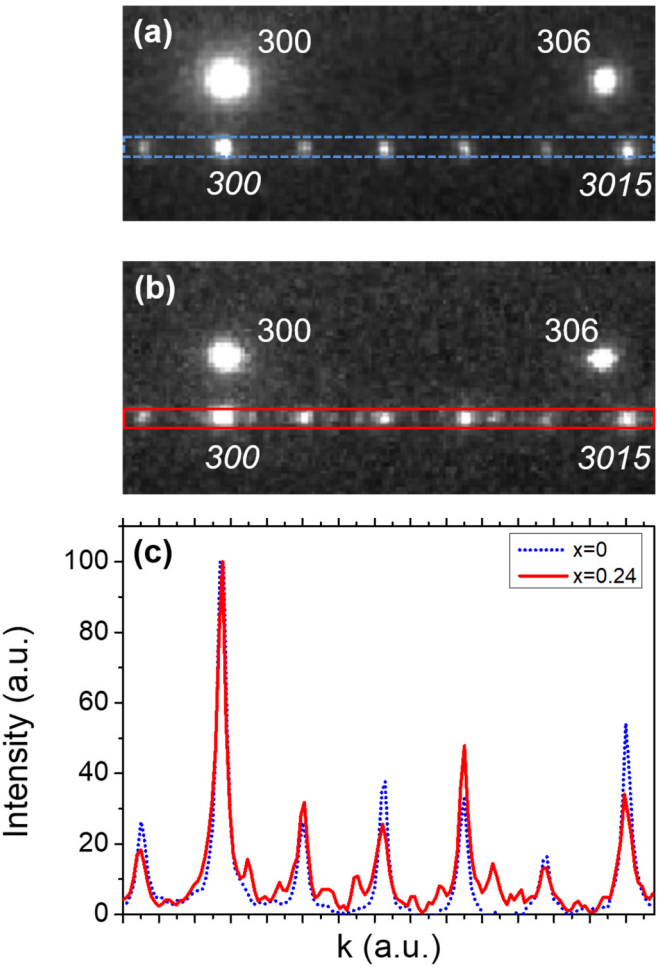

FIG. 3. Electron diffraction with dominant Bragg diffraction in the Sb_2Te_3 film (a) and a mixture of Bragg and diffuse scattering in the $Sb_{0.76}Bi_{0.24}Te_3$ film (b). Line profiles are shown in (c). For $x = 0.24$, additional weak spots between the 300 and 3015 reflections indicate an enlargement of the unit cell in the *c* direction due to Bi/Sb point disorder on *Pn* sites. In addition, the pronounced diffuse scattering streaks reflects thermal disorder in the *c*-lattice parameter. Italic indexing refers to spots of the film, whereas others are diffraction spots from the substrate. (a) and (b) are cutouts from SAED patterns shown in Figs. S6(a) and S6(c) in the Supplemental Material [47].

random distribution of Bi on *Pn* sites. In addition, the diffuse streak like diffracted contrast along (00l) is consistent to thermal diffuse scattering [30,31]. It points to thermal disorder of the *c*-axis lattice parameter, which is a result of strongly anharmonic bonding. This diffuse scattering is also visible in the compilation of the two intensity profiles presented at Fig. 3(c), showing peak broadening and additional shoulders for $x = 0.24$ [for $x = 0.12$ see Fig. S6(b)].

D. Cross-plane lattice thermal conductivity

Figure 4(a) shows the measured temperature dependence of the cross-plane thermal conductivity $\kappa_c(T)$ for all samples. In order to get access to the intrinsic lattice thermal conductivity $\kappa_{c,l}(T)$ of the films, first the contribution of insulation layers as well as the thermal boundary resistances (Kapitza

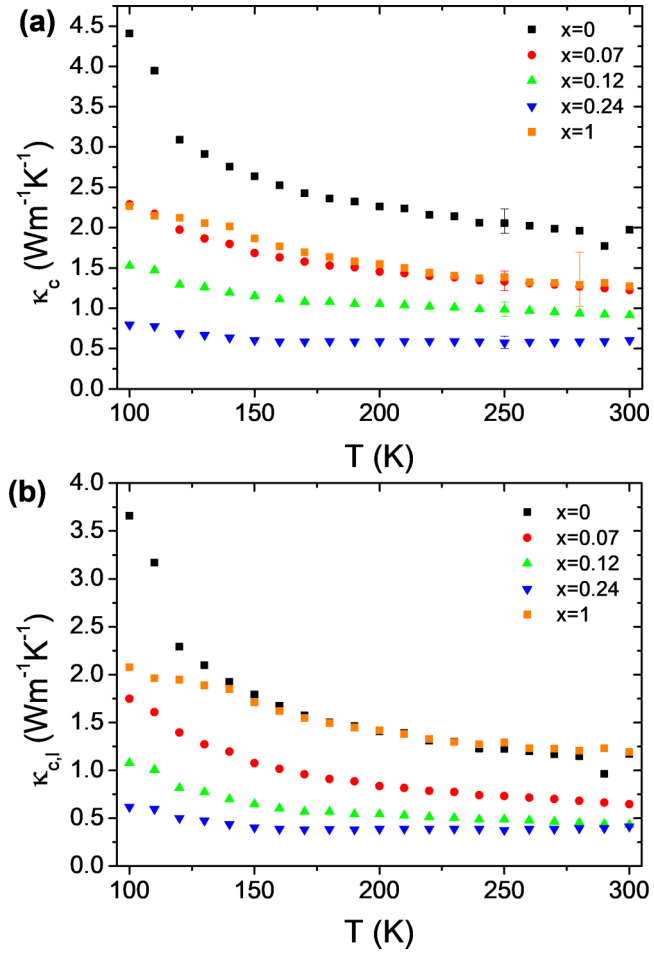

FIG. 4. Thermal conductivity of epitaxial $(Sb_{1-x}Bi_x)_2Te_3$ films along the c axis, obtained from 3ω measurements. (a) Total thermal conductivity $\kappa_c(T)$. (b) Lattice thermal conductivity $\kappa_{c,l}(T)$ after subtraction of the electronic contribution $\kappa_{c,e}(T)$.

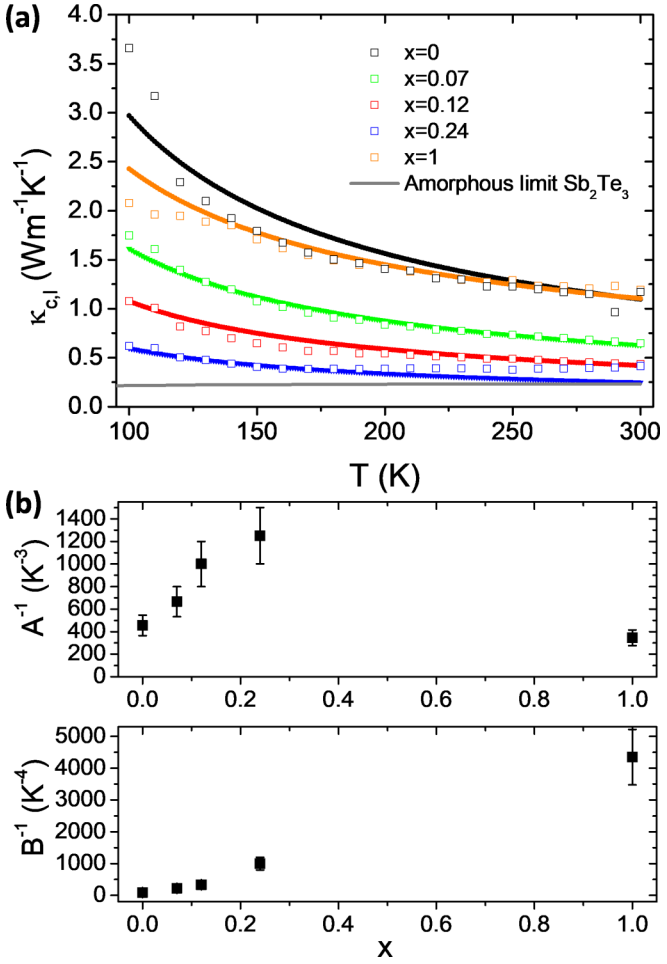

FIG. 5. (a) Comparison of experimental and theoretical temperature dependence of $\kappa_{c,l}(T)$, including the calculated minimum lattice thermal conductivity of Sb_2Te_3 in the c direction. (b) and (c) Show the obtained doping dependence of the scattering strength for umklapp scattering, A^{-1} [Eq. (6)]), and Rayleigh scattering, B^{-1} [Eq. (7)], respectively. Error bars stem from estimated error in the mode dependent density of states used in Eq. (1).

resistances) were subtracted carefully (see Ref. [4]). After subtraction of the electronic contribution $\kappa_{c,e}(T)$ (see Supplemental Material [47]), we obtain the lattice contribution to the thermal conductivity $\kappa_{c,l}(T)$, shown in Fig. 4(b).

Figure 5(a) shows the experimental $\kappa_{c,l}(T)$ data (open symbols) in combination with fits of Eq. (1) in the experimental section (lines in the respective color) for all doping. The minimum lattice thermal conductivity along the c axis for Sb_2Te_3, relevant for $x = 0.24$, is also shown and discussed later. Figures 5(b) and 5(c) show the obtained values of the fit parameters A^{-1} for phonon-phonon scattering and B^{-1} for Rayleigh scattering [Eqs. (6) and (7)], respectively in the experimental section). A^{-1} and B^{-1} in Figs. 5(b) and 5(c) are proportional to the doping dependent scattering rates due to umklapp and Rayleigh scattering, respectively.

E. Relevant phonon frequencies

Figure 6 shows the cumulative lattice thermal conductivity at $T = 100$, 200, and 300 K for two doping levels, $x = 0$ and $x = 0.24$ (see Eqs. (S1) and (S2) in the Supplemental Material [47]). For other doping levels and for the underlying spectral thermal conductivity, see Figs. S10–S14.

The comparison of Figs. 6(a) and 6(b) shows that for the highly Bi doped sample at $x = 0.24$ a higher percentage of the whole $\kappa_{c,l}$ is carried by lower frequency phonons compared to $x = 0$. For example, at 300 K, 90% of the $\kappa_{c,l}$ is carried by phonons up to $\omega = 6600$ and 4600 GHz at $x = 0.0$ and 0.24, respectively. Since the bandgap between A and O modes in Sb_2Te_3 is between 7700 and 8200 GHz in the c direction [23], the contribution of the O modes as well as of the higher frequency A modes to $\kappa_{c,l}$ are suppressed for $x = 0.24$ compared to $x = 0$. Overall one can say that optical phonons only play a minor role in heat transport and do not contribute to thermal conductivity in the solid solutions.

F. Phonon glass state for $x = 0.24$

The obtained temperature characteristics of $\kappa_{c,l}(T)$ for the epitaxial film with $x = 0.24$ deviates from those of the other samples. As shown in Fig. 7, for low temperatures up to $T = 170$ K the phonon model based on Eq. (1) still is well applicable. This is presumably due to the low frequency

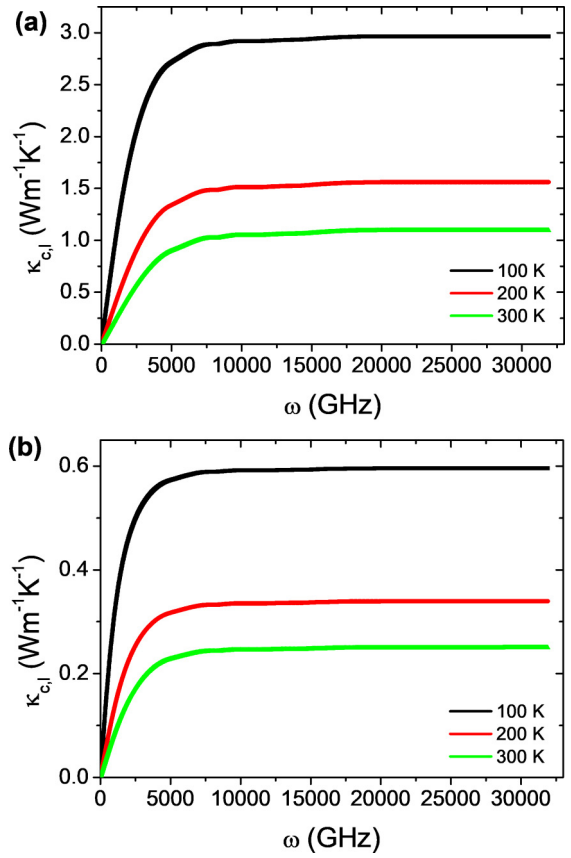

FIG. 6. Lattice thermal conductivity as a function of the upper integration boundary ω at $T = 100$, 200, and 300 K, for (a) $x = 0$ and (b) $x = 0.24$. The transition to saturation gives the upper frequency limit of the phonons contributing to thermal conductivity.

acoustic phonons which dominate $\kappa_{c,l}$ in the low temperature range. At higher temperatures, a plateau, respectively, a very moderate increase in $\kappa_{c,l}(T)$ is observed, that cannot be explained in the phonon picture. It is in contrast to the expected further decrease of $\kappa_{c,l}(T)$ due to an increase of the umklapp

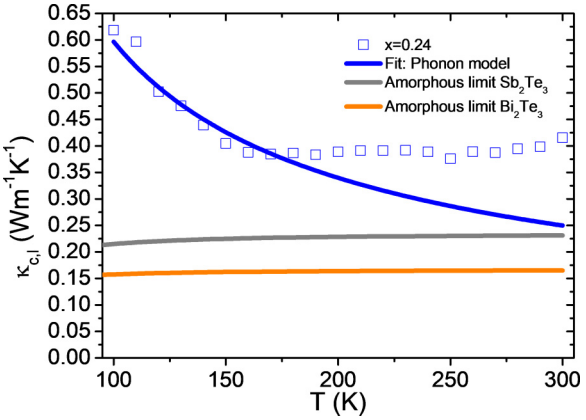

FIG. 7. Experimental lattice thermal conductivity of the epitaxial film with Bi content $x = 0.24$. Blue: Calculated curve within the Callaway model, fitted to the low temperature values of $\kappa_{c,l}(T)$. Grey (Sb_2Te_3) and orange (Bi_2Te_3): Minimum thermal conductivity model for disordered systems with $l_{mfp} = \frac{\lambda}{2}$.

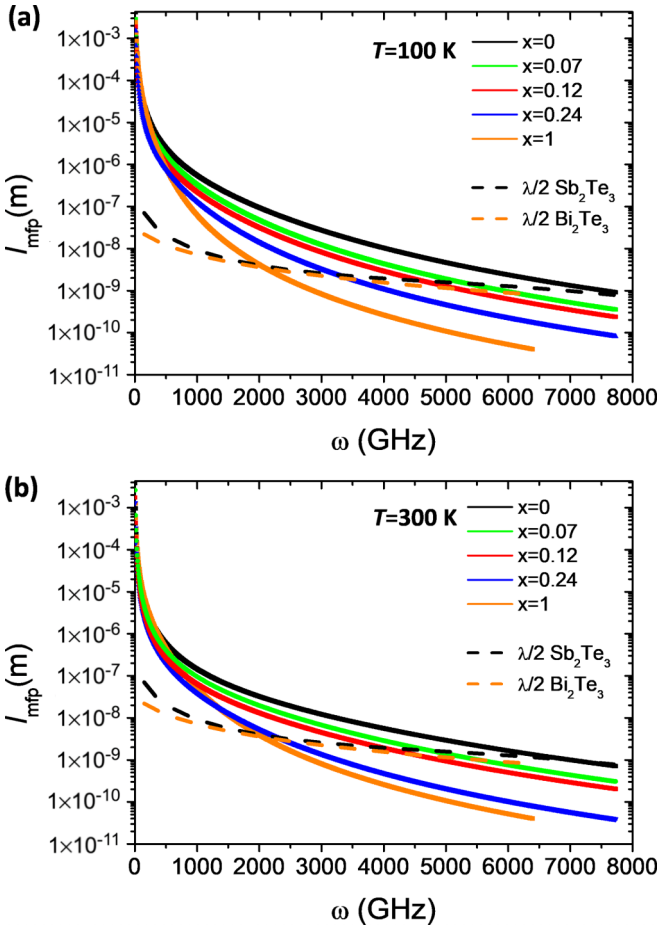

FIG. 8. Phonon mean free path l_{mfp} versus the angular frequency for (a) 100 K and (b) 300 K, as calculated from Eqs. (5), (6), and (7) and using the parameters A^{-1} and B^{-1} in Fig. 5. Additionally, the half phonon wavelength is plotted. At frequencies where $l_{mfp} \leqslant \frac{1}{2}\lambda$ the approximation of phonon quasiparticles as eigenstates of a harmonic periodic lattice break down.

scattering rate with increasing temperature and related phonon population. Consequently, the lattice thermal conductivity of the sample above $T = 150$ K resembles that of an amorphous solid. Using the minimum lattice thermal conductivity model, i.e., Eq. (8) [28], based on the assumption of $l_{mfp} = \frac{\lambda}{2}$, our calculations reveal a temperature independent $\kappa_{c,l}(T)$. We use literature data for the average acoustic phonon velocities of Bi_2Te_3 [18] and Sb_2Te_3 [23] as well as for the lattice parameters of Sb_2Te_3 [32], respectively, Bi_2Te_3 [33]. The minimum thermal conductivity of Bi_2Te_3 is below that of Sb_2Te_3, due to the higher mass of Bi compared to Sb. Both curves are below the experimental curve for the $x = 0.24$ film. This can be either due to the used approximations within the minimum thermal conductivity model. It can predict absolute values of $\kappa_{c,l}(T)$ only with limited accuracy as reviewed by Cahill *et al.* [28]. Furthermore, as indicated by the mean free path in Fig. 8, the possible transition to the phonon glass state might affect only higher frequency modes, whereas l_{mfp} of lower frequency acoustic phonons remain above the $\frac{\lambda}{2}$ threshold. The latter idea is supported by the transition of the temperature dependence of $\kappa_{c,l}(T)$ form the phonon scattering

to the phonon glass regime at a temperature close to the Debye temperature.

G. Phonon mean free path

Figure 8 shows the phonon mean free path versus the angular frequency for all samples. It decreases with increasing Bi content due to increased scattering. The plotted half phonon wavelength gives a rough estimate of the applicability range of the phonon model. For $x = 0.12$ at $T = 300$ K, this is $\omega = 4100$ GHz. Thus, mainly higher frequency A modes can contribute to the c-axis phonon transport, whereas the O modes are in the glass regime. In contrast, for $x = 0.24$, the application limit of the notion of a phonon mean free path shifts down to $\omega = 3000$ GHz. Consequently, also the higher frequency A modes seems to lie in the glass regime, which is now dominant for c-axis thermal transport. For a detailed analysis of the contribution of umklapp $l_{mfp,U}$, respectively, Rayleigh scattering $l_{mfp,R}$ to the total l_{mfp} see Figs. S15 and S16, showing the dominance of umklapp scattering over Rayleigh scattering in the frequency range relevant for thermal transport.

Note that in Fig. 8 for Bi_2Te_3 the obtained $l_{mfp}(\omega, T = 300\,\text{K})$ at $\omega \geqslant 1100$ GHz, is even lower than that of the solid solutions, which is linked to the higher density of states at low frequencies (compare Ref. [23] for Sb_2Te_3 and Ref. [18] for Bi_2Te_3). Furthermore, the relatively high parameter B^{-1} for Bi_2Te_3 indicates a higher density of point defects.

III. DISCUSSION

We first want to focus on the pure material systems Sb_2Te_3 and Bi_2Te_3: The umklapp scattering parameter A^{-1} is similar for both materials, being slightly higher in Sb_2Te_3 compared to Bi_2Te_3. The most significant change is the higher Rayleigh scattering reflected in a high parameter B^{-1}. This might reflect a higher preparation related defect density in the investigated film, due to different growth conditions.

Our results on the doping dependence of the scattering parameters B^{-1} and A^{-1} for Rayleigh and umklapp scattering, respectively, yield an increasing point defect and phonon-phonon scattering with Bi doping x. At $x = 0.12$ the lattice thermal conductivity starts to show a crossover to a temperature independent behavior that is most prominent at $x = 0.24$ for $T > 150$ K. This indicates that higher frequency optical and acoustic phonon modes may have reached the phonon glass limit.

Figure 9 shows the comparison of our data with literature data at 300 K [10,11], obtained by 3ω measurements of MOCVD-grown thin films. At $x = 0$ and $x = 1$ our $\kappa_{c,l}$ values are slightly higher, but close to the literature values within error bars. Note that the measurement error of the literature data is not published. The authors state that they subtracted the thermal conductivity of the used insulation layer. However, heat spread effects enhanced by anisotropy and Kapitza resistances were not considered. Especially for materials with higher κ_c (here: $x = 0$ and $x = 1$), the neglect of the Kapitza resistances results in too low values for κ_c. For the doped samples, our results are in good agreement with the solid solution at $x = 0.25$ [10] as well as with the published

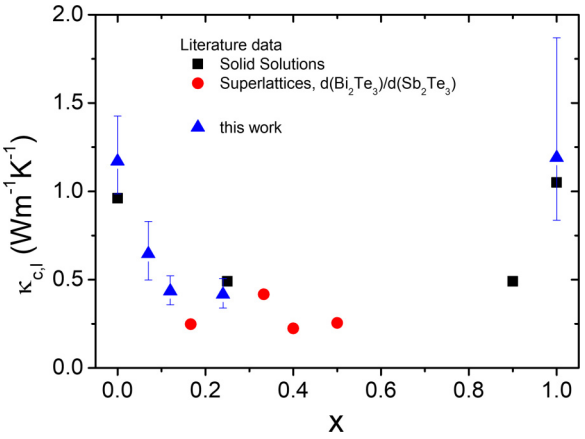

FIG. 9. Comparison of the lattice thermal conductivity in the c direction at $T = 300$ K with literature values for solid solutions [10,11] and for a Sb_2Te_3/Bi_2Te_3 SLs of different bilayer and single layer thicknesses (10/50, 30/60, 20/30, and 30/30 Å) as published by Venkatasubramanian [11].

data of a superlattice (SL) with bilayer thickness of 0.9 nm (0.3 nm Bi_2Te_3/0.6 nm Sb_2Te_3) [11].

The published values for $\kappa_{c,l}$ of SLs with bilayer thicknesses of 0.5 and 0.6 nm are extrapolated from measurements at SLs to a vanishing carrier density. With one exception, they are slightly lower [11] compared to our values for the solid solutions. The difference between alloy and superlattice thermal conductivity has been interpreted as due to phonon blocking effects at the interfaces between the single layers. However, several publications reveal that the growth of SLs with chemically sharp interfaces is inhibited by the required high substrate temperature for epitaxial growth: For sputtered SLs [12], grain growth actually has been observed at 150 °C and for SLs synthesized by molecular beam epitaxy [13], TEM, and XRD data showed that interdiffusion took place at low temperatures of around 200 °C. According to Ref. [34] the samples are synthesized by a MOCVD process with substrate temperatures of around 225 °C, which may be already too high in case of Bi_2Te_3/Sb_2Te_3 SLs: The TEM data presented by Ref. [34] cannot exclude that interdiffusion already has started during sample preparation.

Our results establish that low $\kappa_{c,l}(T) \approx 0.4\ \text{Wm}^{-1}\text{K}^{-1}$ can be reached without elaborate nanostructuring methods at $x = 0.24$. For this doping level, a low and almost constant value of $\kappa_{c,l}(T) \approx 0.39 - 0.42\ \text{Wm}^{-1}\text{K}^{-1}$ is obtained in the temperature range from 160 to 300 K. The low lattice thermal conductivity is found to be an intrinsic material property of the solid solution. Taking into account the solid solution literature data shown in Fig. 9, an almost doping independent and very low value at room temperature seems to be present in a large doping range. Point disorder due to statistical occupation of Pn sites by Bi doping increases the Rayleigh scattering as visible from the doping dependence of $B^{-1}(x)$ in Fig. 5(c). More remarkably, it further increases the umklapp scattering $A^{-1}(x)$ in Fig. 5(b). From the electron diffraction, evidence for the increase of thermal disorder of the c-lattice parameter with doping is consistent with the increase in phonon-phonon scattering and thus to an increase

of the anharmonicity. We cannot separate out, whether this leads to a softening of specific phonon modes or to an amplification of selected phonon scattering channels due to disorder in strongly anharmonic potentials as suggested in Ref. [35].

IV. SUMMARY AND CONCLUSION

In summary, we have performed detailed temperature dependent measurements of the c-axis thermal conductivity in epitaxial, nearly single crystalline $(Sb_{1-x}Bi_x)_2Te_3$ films using the 3ω method. The contribution of Kapitza resistances and the thermal resistance of the used insulation layer were carefully measured and subtracted in order to get the intrinsic $\kappa_c(T)$. Subsequently, we subtracted the electronic contribution by means of literature data receiving the lattice contribution $\kappa_{c,l}(T)$. Theoretical calculations of the c-axis lattice thermal conductivity were performed based on literature data of the density of states and the phonon dispersions in Sb_2Te_3 and Bi_2Te_3. Based on HRTEM results of every studied film, the density of 2D and 3D defects has been found to be negligibly small: Their average distance compares to the $l_{mfp}(\omega)$ only at very low frequencies of $\omega < 1200$ GHz, which do not significantly contribute to $\kappa_{c,l}(T)$. Consequently, umklapp and Rayleigh scattering have been identified as the dominant scattering mechanisms, where umklapp scattering dominates the mean free path in the frequency range relevant for thermal conductivity at room temperature. Remarkably, we obtain both an increase of phonon-phonon scattering as well as of Rayleigh scattering with an increasing substitution of Sb atoms by Bi atoms. The umklapp scattering due to the large anharmonicity of Sb_2Te_3 is slightly higher compared to that of the Bi_2Te_3 film, which is in good agreement with the published Grüneisen parameters [21]. Furthermore, at a doping above $x = 0.12$ a transition of $\kappa_{c,l}(T)$ to a phonon glass sets in, which is most clearly observed for $x = 0.24$ by the anomalous temperature dependence. Based on our results we conclude that the very low lattice thermal conductivities in the solid solution $(Sb_{1-x}Bi_x)_2Te_3$ are intrinsic, caused by the combination of low phonon propagation velocities and small mean free paths. The origin of the latter is mostly the relatively strong anharmonicity further enhanced by Rayleigh scattering.

Due to the epitaxial growth of the epitaxial $(Sb_{1-x}Bi_x)_2Te_3$ films on an insulating Al_2O_3 substrate, direct measurement of cross plane electronic conductivity was not possible. The specific resistance ρ along the c axis of single crystals is $\rho_c = 2.9$–4.6 mΩcm at room temperature [36]. This is one order of magnitude below highly doped Si. Based on the assumption that specific resistance ρ along the c axis of our $x = .24$ film is similarly low, the term "*Phonon glass–electron crystal*" is justified. Clearly, the lattice conductivity is comparably low to a glass, but the sample shows high crystallinity. The combination of low thermal conductivity and high electric conductivity is the origin of good thermoelectric performance around that composition. Such a "*phonon glass–electron crystal*" state can thus be reached in the solid solutions without any nanostructuring methods and our results give rise to further research on doping series in vdW layered thermoelectric materials.

V. METHODS

A. Sample preparation

Epitaxial $(Sb_{1-x}Bi_x)_2Te_3$ thin films were deposited on Al_2O_3 (0001) [$10 \times 10 \times 0.5$ mm] substrates using a vertical PVD system that was previously described elsewhere [37]. Mixtures of commercial Sb_2Te_3 (99.999% abcr GmbH) and Bi_2Te_3 powders (99.99% abcr GmbH) were used in various ratios as precursor material. The film deposition was performed at constant substrate (330 °C) and evaporator temperatures (570 °C) for epitaxial Sb_2Te_3 and $(Sb_{1-x}Bi_x)_2Te_3$ thin films on Al_2O_3 (0001) substrates. Successful growth of c-oriented highly crystalline films was possible in the doping range $x = 0$, 0.07, 0.12, 0.24, respectively, at a working pressure of 20 mbar. In addition, highly crystalline, epitaxial Bi_2Te_3 films were grown on Al_2O_3 (0001) substrates at a substrate temperature of 290 °C and evaporator temperature of 605 °C under high vacuum conditions (10^{-4} mbar). The growth parameters are summarized in Table S1 in the Supplemental Material. XRD studies were performed with a Bruker D8 Advance powder diffractometer in a Bragg-Brentano geometry, using a Cu-$K\alpha$ radiation ($\lambda = 1.5418$ Å). The chemical composition of the resulting binary and ternary material films was determined by energy dispersive x-ray and the results are given in Table S2.

B. HRSTEM investigations

Sample preparation for TEM analysis was carried out by a focused ion beam, using a FEI Nova NanoLab 600. Due to the pronounced beam sensitivity of the vdW layered material, a dedicated preparation procedure was applied to obtain high quality TEM lamellas with minimized thin amorphous top layer. Rough cutting and thinning steps were done at 30 kV followed by a thinning step at a beam voltage of 5 kV. HRTEM and STEM investigations were performed at an aberration (C_S) corrected FEI Titan 80–300 kV operated at 300 kV. HRTEM studies were done for all differently doped samples. An interface analysis of the Sb_2Te_3 film via HRTEM, STEM and Electron Energy Loss Spectroscopy is published in Ref. [4].

C. HRSTEM simulations

HRSTEM images show random distribution of individual atomic columns or parts of the corresponding lattice planes occupied with Sb and Bi with the enhanced contrast. This effect was reproduced by the HRSTEM image simulations using a QSTEM software package [38]. A box of $8 \times 8 \times 15$ nm was filled with Sb_2Te_3 or Bi_2Te_3 unit cells. In order to reproduce mixed compositions, randomly selected 12 or 24 percent of Sb atoms were replaced with Bi atoms. Simulation parameters were chosen as listed in Table S3.

D. Thermal conductivity measurements

The cross-plane thermal conductivity $\kappa_c(T)$ of the $(Sb_{1-x}Bi_x)_2Te_3$ films on Al_2O_3 (0001) was measured in a temperature range from 100 to 300 K by a self-built 3ω setup, using a modified offset method [39]. Here, the absolute value of the temperature oscillation in the heater structure $|\Delta T|(\omega)$

was measured as a function of the angular frequency. The slope of $|\Delta T|(\omega)$ determines the thermal conductivity of the substrate and thus was used to calculate the contribution of the temperature oscillation $|\Delta T_s|(\omega)$ due to the substrate, only (exemplary data see Fig. S17). The thermal conductivity of the film was then determined from $|\Delta T_f|(\omega) = |\Delta T|(\omega) - |\Delta T_s|(\omega)$, where the contributions of the ion beam sputtered SiO_2 layer for electrical insulation of the Pt-heater structure as well as the thermal boundary resistances (Kapitza resistances) have been carefully determined and subtracted. This has been done on the basis of measurement of $|\Delta T|$ for varying SiO_2 and for varying Sb_2Te_3 thickness. For details regarding Kapitza resistance, sample geometry, and the applied 3ω method see Ref. [4]. The formulas used for considering horizontal heat spread in the film require values for the anisotropy η of κ. The used value for $x = 0$ was $\eta = 2.3$ [4] and $\eta = 1.59$ for $x = 0.25$ [40]. For $x = 0.07 - 0.24$ an interpolation of $\eta(x)$ between $x = 0$ and $x = 0.25$ has been used and for $x = 1$, the anisotropy of $\eta = 2.3$ has been obtained from Ref. [41].

E. Lattice thermal conductivity calculations

In order to develop a better understanding of the fundamental mechanisms that determine the phonon heat transport in $(Sb_{1-x}Bi_x)_2Te_3$, lattice thermal conductivity calculations and fitting to the experimental data was performed using MATLAB. For every temperature, the sum over all phonon modes n was calculated by

$$\kappa_{c,l}(T) = \sum_{n1}^{n2} \int_{\omega_{\min}}^{\omega_{\max}} g(\omega) C(\omega, T) v_n(\omega) l_{mfp}(\omega, T) d\omega, \quad (1)$$

where $g(\omega)$ is the density of states per angular frequency ω $v_n(\Omega)$ is the velocity of sound of a specific phonon mode n, $C(\omega, T)$ is the specific heat, and $l_{mfp}(\omega, T)$ is the frequency and temperature dependent mean free path. The density of states $g(\omega)$ was obtained from experimental neutron incoherent scattering data [42] of Sb_2Te_3 and Bi_2Te_3, fitted by polynomials, see Fig. S18 in the Supplemental Material. In order to get the absolute values needed for our calculations, the total density of states curve $g(\omega)$ was scaled to an absolute value of

$$g(\omega_D) = \frac{3}{2\pi^2 v_c^3} \cdot \omega_D^2 \quad (2)$$

at the Debye frequency ω_D, which is given by

$$\omega_D = \frac{k\Theta_D}{\hbar} = 21,6\ \text{THz}. \quad (3)$$

This value was taken for all samples because of $\Theta_D = 165$ K for Sb_2Te_3 [43] and Bi_2Te_3 [44]. Since Eq. (1) sums up over single phonon modes and Fig. S18 gives the overall $g(\omega)$, we use only the frequency range where c-axis modes contribute and take into account the overlap to in-plane modes by $g(\omega)/\chi$, where $\chi \approx 9$ due to three crystallographic directions and the presence of three phonon modes per frequency. This coarse approximation is justified since the Callaway theory disregards the anisotropy, however, as discussed in Ref. [4], for moderate anisotropies in the range of 2–3, the resulting error in the mean free path is with 20–30% rather small. This might be a minor error in comparison to the used models for the frequency dependent scattering, Eqs. (6) and (7).

The specific heat capacity per phonon $C(\omega, T)$ is expressed by

$$C(\omega, T) = \frac{(\hbar\omega)^2}{k_B T^2} \frac{\exp\left(\frac{\hbar\omega}{k_B T}\right)}{\left(\exp\left(\frac{\hbar\omega}{k_B T}\right) - 1\right)^2}. \quad (4)$$

The velocity of sound $v_n(\omega)$ of a specific phonon mode n at a specific angular frequency ω as well as the minimal and maximal frequencies of a specific phonon mode, $\omega_{\min}$ and $\omega_{\max}$, were obtained from first principles calculations of the phonon dispersion relations of Sb_2Te_3 [23] and Bi_2Te_3 [18], respectively. For all samples, except $x = 1$, the phonon dispersion relations of Sb_2Te_3 were used. This is justified from the experimental observation that the solid solutions do not alter the symmetry of the crystal lattice and the qualitative similarity of the phonon dispersion relations for $x = 0$ and $x = 1$. The obtained average velocity of acoustic phonon modes is in good agreement with sound velocities v_c deduced from Stiffness matrices [45] and mass densities [46], yielding $v_c = 1383\,\text{ms}^{-1}$ for Sb_2Te_3 and $v_c = 1057\,\text{ms}^{-1}$ for Bi_2Te_3, see Fig. S19 in the Supplemental Material.

For the total phonon mean free path $l_{mfp}(\omega, T)$ we used a combination of umklapp scattering and Rayleigh scattering, summed up according to the Matthiessen rule,

$$l_{mfp}(\omega, T) = \frac{1}{\frac{1}{l_{mfp,U}} + \frac{1}{l_{mfp,R}}}. \quad (5)$$

For umklapp and Rayleigh scattering we have used the following analytical approximations [27]:

$$l_{mfp,U} = A\left(\frac{k_B}{\hbar\omega}\right)^2 \frac{1}{T} \exp\left(\frac{\Theta_D}{3T}\right), \quad (6)$$

$$l_{mfp,R} = B\left(\frac{k_B}{\hbar\omega}\right)^4. \quad (7)$$

The parameters A and B are obtained by fitting the calculated $\kappa_{c,l}(T)$ curve to the experimental data. These semiempirical equations have been justified by comparison with experimental thermal conductivity in semiconductors.

Based on the Debye model, Cahill *et al.* [28] assumed a random walk between localized quantum mechanical oscillators to determine the minimum lattice thermal conductivity. We use the resulting expression, Eq. (8), to calculate the minimum lattice thermal conductivities of Sb_2Te_3 and Bi_2Te_3, respectively. This expression only requires the density of atoms n and the speed of sound v_i for two transverse and one longitudinal mode. Equation (9) determines the respective cutoff frequencies $k_B\Theta_i = \hbar\omega$ using the Debye approximation (See Supplemental Material [47]):

$$\kappa_{\min} = \left(\frac{\pi}{6}\right)^{\frac{1}{3}} k_B n^{\frac{2}{3}} \sum_i v_i \left(\frac{T}{\Theta_i}\right)^2 \int_0^{\frac{\Theta_i}{T}} \frac{x^3 e^x}{(e^x - 1)^2} dx, \quad (8)$$

$$\Theta_i = v_i \left(\frac{\hbar}{k_B}\right) (6\pi^2 n)^{\frac{1}{3}}. \quad (9)$$

ACKNOWLEDGMENTS

Financial support by the Deutsche Forschungsgemeinschaft DFG (S.S., Project No. SCHU 1069/20-1; C.J., Project No. JO 348/12-1), as well as by SFB 1073 is gratefully acknowledged.

[1] Edited by C. Uher, *Materials Aspect of Thermoelectricity* (Taylor & Francis, London, 2017).
[2] H. J. Goldsmid and R. W. Douglas, Br. J. Appl. Phys. **5**, 386 (1954).
[3] M. Z. Hasan and C. L. Kane, Rev. Mod. Phys. **82**, 3045 (2010).
[4] F. Rieger, K. Kaiser, G. Bendt, V. Roddatis, P. Thiessen, S. Schulz, and C. Jooss, J. Appl. Phys. **123**, 175108 (2018).
[5] C. V. Manzano, B. Abad, M. Muñoz Rojo, Y. R. Koh, S. L. Hodson, A. M. Lopez Martinez, X. Xu, A. Shakouri, T. D. Sands, T. Borca-Tasciuc, and M. Martin-Gonzalez, Sci Rep. **6**, 19129 (2016).
[6] C. Zhang, Z. Peng, Z. Li, L. Yu, K. A. Khor, and Q. Xiong, Nano Energy **15**, 688 (2015).
[7] F. Serrano-Sánchez, M. Gharsallah, N. M. Nemes, N. Biskup, M. Varela, J. L. Martínez, M. T. Fernández-Díaz, and J. A. Alonso, Sci. Rep. **7**, 6277 (2017).
[8] J. R. Drabble and C. H. L. Goodman, J. Phys. Chem. Solids **5**, 142 (1958).
[9] D. Lencer, M. Salinga, B. Grabowski, T. Hickel, J. Neugebauer, and M. Wuttig, Nat. Mater. **7**, 972 (2008).
[10] R. Venkatasubramanian, E. Siivola, T. Colpitts, and B. O'Quinn, Nature (London) **413**, 597 (2001).
[11] R. Venkatasubramanian, Phys. Rev. B **61**, 3091 (2000).
[12] M. Winkler, X. Liu, A.-L. Hansen, J. D. König, W. Bensch, L. Kienle, H. Böttner, and K. Bartholomé, Nanothermoelectrics **1**, 1 (2013).
[13] A.-L. Hansen, T. Dankwort, M. Winkler, J. Ditto, D. C. Johnson, J. D. König, K. Bartholomé, L. Kienle, and W. Bensch, Chem. Mater. **26**, 6518 (2014).
[14] For a recent review article see,T. Dankwort, A.-L. Hansen, M. Winkler, U. Schürmann, J. D. Koenig, D. C. Johnson, N. F. Hinsche, P. Zahn, I. Mertig, W. Bensch, and L. Kienle, Phys. Status Solidi A **213**, 662 (2016).
[15] M. Winkler, X. Liu, U. Schürmann, J. D. König, L. Kienle, W. Bensch, and H. Böttner, Z. Anorg. Alleg. Chem. **638**, 2441 (2012).
[16] D. Das, S. Das, P. Singha, K. Malik, A. K. Deb, A. Bhattacharyya, V. A. Kulbachinskii, R. Basu, S. Dhara, S. Bandyopadhyay, and A. Banerjee, Phys. Rev. B **96**, 064116 (2017).
[17] Y. Tian, S. Jia, R. J. Cava, R. Zhong, J. Schneeloch, G. Gu, and K. S. Burch, Phys. Rev. B **95**, 094104 (2017).
[18] O. Hellman and D. A. Broido, Phys. Rev. B **90**, 134309 (2014).
[19] C. K. Gan and C. H. Lee, Comput. Mater. Sci. **151**, 49 (2018).
[20] K. H. Park, M. Mohamed, Z. Aksamija, and U. Ravaioli, J. Appl. Phys. **117**, 015103 (2015).
[21] D. Bessas, I. Sergueev, H.-C. Wille, J. Perßon, D. Ebling, and R. P. Hermann, Phys. Rev. B **86**, 224301 (2012).
[22] S. Lee, K. Esfarjani, T. Luo, J. Zhou, Z. Tian, and G. Chen, Nat. Commun. **5**, 3525 (2014).
[23] B.-T. Wang, P. Souvatzis, O. Eriksson, and P. Zhang, J. Chem. Phys. **142**, 174702 (2015).
[24] N.-W. Park, W.-Y. Lee, J.-E. Hong, T.-H. Park, S.-G. Yoon, H. Im, H. S. Kim, and S.-K. Lee, Nanoscale Res. Lett. **10**, 20 (2015).
[25] P. Lošťák, Č. Drašar, A. Krejčová, L. Beneš, J. S. Dyck, W. Chen, and C. Uher, J. Cryst. Growth **222**, 565 (2001).
[26] P. Lošťák, Č. Drašar, J. Horàk, Z. Zhou, J. S. Dyck, and C. Uher, J. Phys. Chem. Sol. **67**, 1457 (2006).
[27] J. Callaway, Phys. Rev. **113**, 1046 (1959).
[28] D. G. Cahill, S. K. Watson, and R. O. Pohl, Phys. Rev. B **46**, 6131 (1992).
[29] G. A. Slack, Solid State Phys. **34**, 1 (1979).
[30] C. R. Hall and P. B. Hirsch, Proc. R. Soc. A **286**, 158 (1965).
[31] Z. L. Wang, Philos. Mag. B **65**, 559 (1992).
[32] W.-S. Kim, J. Alloys Compd. **252**, 166 (1997).
[33] Y. Feutelais, B. Legendre, N. Rodier, and V. Agafonov, Mater. Res. Bull. **28**, 591 (1993).
[34] R. Venkatasubramanian, T. Colpitts, B. O'Quinn, S. Liu, N. El-Masry, and M. Lamvik, Appl. Phys. Lett. **75**, 1104 (1999).
[35] P. Erhart, P. Hyldgaard, and D. O. Lindroth, Chem. Mater. **27**, 5511 (2015).
[36] H. Scherrer and S. Scherrer, *CRC Handbook of Thermoelectrics*, edited by D. M. Rowe (CRC Press, Boca Raton, FL, 1995), Chap. 19, p. 221.
[37] G. Bendt, K. Kaiser, A. Heckel, F. Rieger, D. Oing, A. Lorke, N. Perez Rodriguez, G. Schierning, C. Jooss, and S. Schulz, Semicond. Sci. Technol. **33**, 105002 (2018).
[38] C. Koch, Ph.D. dissertation, Arizona State University, 2002.
[39] P. Thiessen, V. Roddatis, F. Rieger, A. Belenchuk, M. Keunecke, V. Moshnyaga, and Ch. Jooss, Phys. Rev. B **98**, 195114 (2018).
[40] A. Jacquot, N. Farag, M. Jaegle, M. Bobeth, J. Schmidt, D. Ebling, and H. Böttner, J. Electron. Mater. **39**, 1861 (2010).
[41] H. J. Goldsmid, Proc. Phys. Soc. B **69**, 203 (1956).
[42] H. Rauh, R. Geick, H. Köhler, N. Nücker, and N. Lehner, J. Phys. C **14**, 2705 (1981).
[43] X. X. Yang, Z. F. Zhou, Y. Wang, R. Jiang, W. T. Zhen, and Ch. Q. Sun, J. Appl. Phys. **112**, 083508 (2012).
[44] J. O. Jenkins, J. A. Rayne, and R. W. Ure, Jr., Phys. Rev. B **5**, 3171 (1972).
[45] M. de Jong, W. Chen, T. Angsten, A. Jain, R. Notestine, A. Gamst, M. Sluiter, C. Krishna Ande, S. van der Zwaag, J. J. Plata, C. Toher, S. Curtarolo, G. Ceder, K. A. Persson, and M. Asta, Sci. Data **2**, 150009 (2015).
[46] W. M. Haynes, *CRC Handbook of Chemistry and Physics*, 97th ed. (CRC Press, Boca Raton, FL, 2016).
[47] See Supplemental Material at http://link.aps.org/supplemental/10.1103/PhysRevMaterials.4.025402 for Tables S1–S3, giving information on film preparation and image simulation, as well as Figs. S1–S19, showing additional structural analysis and properties relevant to thermal transport.